The Astrophysical Journal, 889:57 (11pp), 2020 January 20 https://doi.org/10.3847/1538-4357/ab5dbe

Effects of 150–1000 eV Electron Impacts on Pure Carbon Monoxide Ices Using the Interstellar Energetic-Process System (IEPS)

C.-H. Huang[1], A. Ciaravella[2], C. Cecchi-Pestellini[2], A. Jiménez-Escobar[2], L.-C. Hsiao[1], C.-C. Huang[1], P.-C. Chen[1], N.-E. Sie[1], and Y.-J. Chen[1]
[1] Department of Physics, National Central University, Jhongli District, Taoyuan City 32054, Taiwan; chhuang@phy.ncu.edu.tw, asperchen@phy.ncu.edu.tw
[2] INAF—Osservatorio Astronomico di Palermo, P.za Parlamento 1, I-90134 Palermo, Italy
Received 2019 July 22; revised 2019 November 11; accepted 2019 November 26; published 2020 January 24

Abstract

Pure CO ice has been irradiated with electrons of energy in the range 150−1000 eV with the Interstellar Energetic-Process System. The main products of irradiation are carbon chains C_n ($n = 3, 5, 6, 8, 9, 10, 11, 12$), suboxides, C_nO ($n = 2, 3, 4, 5, 6, 7$), and C_nO_2 ($n = 1, 3, 4, 5, 7$) species. CO_2 is by far the most abundant reaction product in all the experiments. The destruction cross section of CO peaks at about 250 eV, decreases with the energy of the electrons and is more than one order of magnitude higher than for gas-phase CO ionization. The production cross section of carbon dioxide has been also derived and is characterized by the competition between chemistry and desorption. Desorption of CO and of new species during the radiolysis follows the electron distribution in the ice. Low-energy electrons having short penetration depths induce significant desorption. Finally, as the ice thickness approaches the electron penetration depth the abundance of the products starts to saturate. Implications on the atmospheric photochemistry of cold planets hosting surface CO ices are also discussed.

Unified Astronomy Thesaurus concepts: Astrochemistry (75); Protoplanetary disks (1300); Laboratory astrophysics (2004)

1. Introduction

Carbon monoxide is the dominant carbon reservoir in molecular gas, and among the most abundant molecules in the Universe. Interstellar CO ice, distinctive from gaseous molecules, was first positively identified in 1984 with the detection of infrared absorption at 4.67 μm in several molecular clouds (Lacy et al. 1984). Such detection occurred a decade after the discovery of interstellar water ice observed toward the embedded protostellar Becklin–Neugebauer object by Gillett & Forrest (1973). Subsequent observations suggested that ices containing CO were ubiquitous in cold interstellar and circumstellar regions (Herbst & van Dishoeck 2009). These astronomical observations stimulated intense activity in laboratory studies of solid-state chemistry that, together with accurate observational results, gave rise to the current description of ices in space. We know that the onset of CO ice occurs in darker regions than those in which the onset of water ice occurs (Boogert et al. 2015). Water ice deposition is mostly completed before the CO ice is deposited on the dust grains. Therefore, interstellar ices appear to have a layered structure surrounding the dust grain cores: an inner water-rich layer forms early in the evolution of a cloud by hydrogenation of oxygen, frozen at the grain surface, and solid methane and ammonia are also likely to be formed in surface reactions at this stage, through hydrogenation of carbon and nitrogen. During the initial stages of star formation, the increase in gas density is so steep that the freeze-out timescale shortens dramatically, inducing a catastrophic removal of the gas, whose main component is carbon monoxide. The formation of the CO ice layer provides the raw material from which icy methanol and other species may be formed (Chuang et al. 2016).

Carbon monoxide is known to be present as ice on planetary and moon surfaces such as Triton (Lellouch et al. 2010)—presumably a captured Kuiper Belt object—and Pluto (Bertrand & Forget 2016), and supposed to be present in exoplanetary cryospheres (Beaulieu et al. 2006).

Many types of radiation fields ubiquitous in interstellar and circumstellar regions can chemically process carbon monoxide, giving rise to a variety of effects going from chemical evolution to photodesorption. Jamieson et al. (2006) present a detailed discussion of energetic particle bombardment. To simulate the energetic electrons trapped in magnetospheres of planets and to reproduce the irradiation effects of typical Galactic cosmic-ray particles, these authors performed experiments in which CO ices kept at cryogenic temperatures were irradiated with (moderately) energetic keV electrons. In this work, we exploit electrons in the energy middle-range (150–1000 eV), to explore the effects at energies closer to mean energies of primary electrons produced by cosmic-rays (Cecchi-Pestellini & Aiello 1992) and X-rays (Tiné et al. 1997) impacting with molecular gas.

The electrons used in this work lose 99% of their energy within 52.5 nm inside the CO ice. This penetration depth is much shorter than the 690 nm required for the 5 keV electrons employed by Jamieson et al. (2006), the ∼440 nm of the ultraviolet photons (Cruz-Diaz et al. 2014), and the ∼2500 nm of 550 eV X-rays (Ciaravella et al. 2016).

In Section 2 we present the experimental facility used in this work. We describe our experiments in Section 3, illustrate the results in Section 4, and discuss them in Section 5. The last section contains our conclusions.

2. Experimental Facility

The experiments reported in this work have been performed with the Interstellar Energetic-Process System (IEPS, National Central University, Taiwan). IEPS is an ultra-high vacuum (UHV) chamber equipped with radiative sources, a pre-mixing system, and detection/diagnostic instruments. A schematic picture of IEPS is shown in Figure 1. The facility is detailed below.

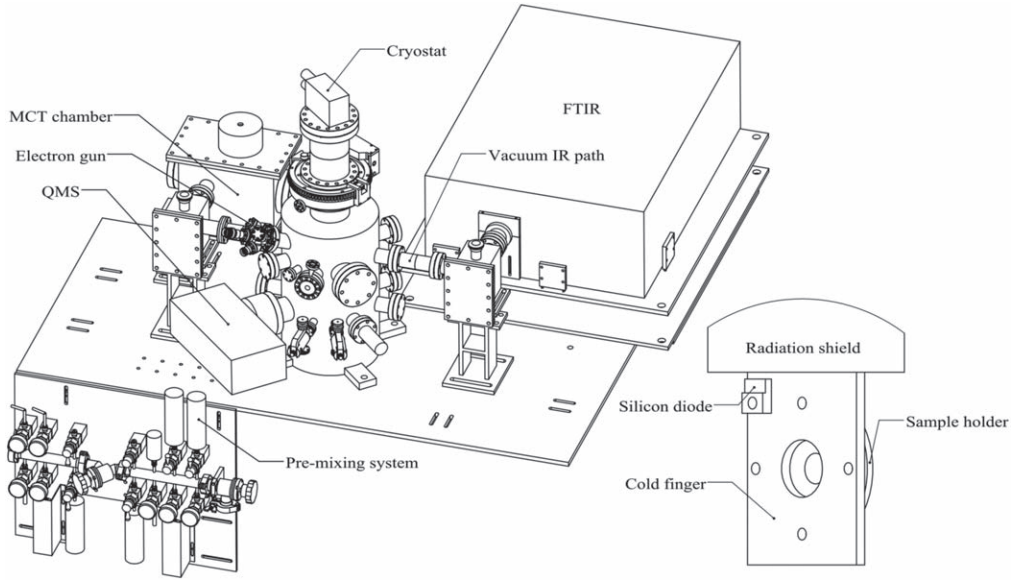

Figure 1. IEPS UHV experimental setup. In the right inset some details of the cold finger assembly are reported.

2.1. UHV Chamber

The base pressure inside IEPS, measured by an ion gauge (Granville-Phillips 370 Stabil), is $\lesssim 5 \times 10^{-10}$ torr. The vacuum is obtained with a turbo-molecular pump (Oerlikon Leybold vacuum 600C, 600 l s^{-1}), backed up by a scroll pump (Edward nXDS15i). A closed-cycle helium cryostat (CTI M350), is mounted on a rotating platform (Thermionics RNN-400 equipped with stepper motor) at the center of the chamber, see Figure 1. At the end of the cold finger there is a sample holder (see the inset in Figure 1), where an infrared transparent window can be mounted as substrate for the ices. Two temperature sensors driven by a Lakeshore 335 temperature controller are mounted along the cold finger. The first one is close to the sample holder (Lakeshore DT-670-OB), while the other is located on tip of the second stage of the cryostat (Lakeshore DT-470-SD). The cold finger and copper radiation shield are placed on the second and first stages of the cryostat, respectively. A heater is hooped on the cold finger and operated through the temperature controller. In order to improve thermal conductivity, all junctions are made with indium (99.99% purity). The infrared transparent window is housed in the sample holder of the cryostat. The window is held by a circular copper ring tightened by screws with spring washers to avoid damaging the window at low temperatures. In this configuration, the substrate can be maintained at temperatures in the range of 11–340 K with an uncertainty of ± 0.3 K. The infrared and ultraviolet sources are 45° incident on the sample holder. IEPS is designed to allow simultaneous irradiation with different energetic sources. In the present configuration, there is an electron gun (Kimball physics EFG-7 equipped with EGPS-2017 power supply) and a T-type (Chen et al. 2014) microwave-discharge hydrogen-flow lamp (Opthos Instruments, INC.).

2.2. Pre-mixing System

Gas mixtures are prepared in the stainless steel pre-mixing system made of two gas-lines containing four bottles of equal volumes. The system is pumped by a turbo-molecular pump (Oerlikon Leybold 361, 400 l s^{-1}) backed up by an oil-sealed mechanical pump (Alcatel 2012A) equipped with an oil trap containing molecular sieves (type 13X). The system is baked at 100° C to obtain optimal vacuum conditions, and eliminate contamination. The base pressure is 8×10^{-8} torr. The partial pressures of the gas components are measured by a capacitance manometer (BROOKS CMC series working in the range of 0–100 torr with 0.5% accuracy). The prepared gas sample is introduced into the UHV chamber through a leak valve (VG, ZLVM 940R) connected to a 1/16 inch stainless tube pointed toward the cold substrate.

2.3. Detection System

A Fourier Transform (mid-)InfraRed (FTIR) spectrometer (Bruker VERTEX 70), and a Quadrupole Mass Spectrometer (QMS, Hiden analysis/3F RC PIC) are the diagnostic instruments. The FTIR spectrometer is equipped with a Mercury–Cadmium–Tellurium (MCT) detector that records transmission spectra of the ice sample. To reduce the absorbance of gas-phase CO_2 and H_2O in the atmosphere, the infrared beam is introduced into a vacuum path separated from UHV by two wedged ZnSe window flanges, located at the entrance and exit sides of the UHV chamber. The MCT detector is kept in a rectangular vacuum chamber. The QMS is mounted with its central axis pointed along the normal direction of the substrate. The emission current of the QMS filament and integrated scanning time can be manually regulated. The exploited emission current is 100 μA, and the scanning time 100 ms for each mass. The electron-impact ionization energy has been chosen to be 70 eV. The minimal partial pressure detectable by the QMS is 3.5×10^{-15} torr.

3. Experiments

The experiments consist of three phases: deposition, irradiation, and warm-up. The CO gas (CINGFONG GAS INDUSTRIAL, purity 99.99%), prepared in the pre-mixing chamber at 5 torr, is introduced in the UHV chamber at a pressure of 10^{-7} torr for about 20 minutes, and condensed on a CaF_2 window cooled at 11 K. At the end of the deposition we wait 30 minutes in order to obtain vacuum conditions similar to those before deposition.

We compute the ice thickness ΔL using the 2136 cm^{-1} feature of CO with a band strength $A = 1.1 \times 10^{-17}$ cm molecules^{-1}

Table 1
Experimental Parameters

Electr. Energy (eV)	Irrad. Time (s)	Dose (eV molecule^{-1})	Abs. Elec. (electron cm^{-2})	Abs. Ener. (eV cm^{-2})	Λ_e (ML/nm)
150	3095	27.5	1.0×10^{15}	1.5×10^{17}	8.5/3.8
200	6095	45.6	1.9×10^{15}	3.9×10^{17}	12.8/5.8
250	4715	32.8	1.5×10^{15}	3.8×10^{17}	17.2/7.8
300	3095	20.4	1.1×10^{15}	3.3×10^{17}	21.8/9.9
400	2675	16.2	8.7×10^{14}	3.5×10^{17}	31.8/14.4
500	2305	13.0	7.6×10^{14}	3.8×10^{17}	42.8/19.3
600	1985	10.3	6.5×10^{14}	3.9×10^{17}	55.3/25.0
800	1465	6.7	4.8×10^{14}	3.9×10^{17}	83.6/37.8
1000	1255	5.2	4.1×10^{14}	4.1×10^{17}	116.2/52.5

(Jiang et al. 1975). The CO column density measured in monolayers (1 ML = 1×10^{15} molecules cm^{-2}) along the infrared beam is calculated as

$$\Delta L_{\rm IR} = \frac{1}{A} \int_{\Delta\nu} \tau_\nu d\nu, \quad (1)$$

where τ_ν is the optical depth of the band, and $\nu\,{\rm cm}^{-1}$ the wavenumber. In all the experiments the ice thickness is measured to be $\Delta L = 707$ ML (319 nm). The infrared and electron beams impinge the ice surface at 45° and 25°, respectively. Therefore, the effective ice thickness is 1000 ML (452 nm) along the infrared beam, and 781 ML (353 nm) along the electrons beam. In the following, unless otherwise specified, column densities refer to the direction along the electron beam. The major error on the ice thickness is dominated by the uncertainty in the band strength, i.e., 9.5% (Jiang et al. 1975).

The infrared spectra collected before and during the irradiation are obtained using 2 cm^{-1} resolution. At the end of the radiolysis the ice is warmed up to room temperature at a rate of 2 K minutes^{-1}. During this phase, infrared spectra have been collected every 5 K starting from 15 K, with 2 cm^{-1} resolution.

The QMS monitored gas species in the chamber from $m/z = 12$ to 100, for the entire duration of the experiments. During the warm-up, the mass $m/z = 28$, related to CO, has been excluded because its intensity can be higher than the safe ion counts limit (10^7 ion counts s^{-1}) of the QMS.

The radiolysis of pure CO ice is performed using electrons of energies from $E_e = 150$ to 1000 eV, and a flux of $f = 3.2 \times 10^{11}$ electron cm^{-2} s^{-1}. The energy uncertainty is 0.02%. The spot size is 2 ± 0.1 cm^2. The irradiation time is chosen to have similar total impinging energy in all the experiments. For the lowest energy case, $E_e = 150$ eV, we stopped the irradiation earlier because the abundances of products do not vary appreciably after three long ($\Delta t = 1000$ s) irradiation steps.

The experiments, repeated at least two times, are summarized in Table 1. The columns in the table list the electron energies used in the experiments, the total irradiation times, the total absorbed electrons, the total absorbed energies, and the penetration length along the direction of the electron beam, Λ_e. We characterize each electron energy through a penetration length defined as the depth within the ice at which the electrons loose 99% of their initial energies. The penetration lengths are estimated with "monte CArlo SImulation of electroN trajectory in sOlids" (CASINO) software (Drouin et al. 2007) using a CO ice density $\delta_{\rm CO} = 1.0288$ g cm^{-3} (Jiang et al. 1975). The statistic error on the penetration depth is 0.1%.

4. Results and Analysis

4.1. Products of the Irradiations

Figure 2 shows the infrared spectra after the CO ices has been irradiated with the same number of impinging electrons, 2.2×10^{14} electrons cm^{-2}.

The impinging electrons ionize CO molecules, producing a cascade of secondary electrons. The net effect is ionization, excitation, and dissociation of CO molecules, and the injection of reactive ions, atoms, and molecules into the ice. Below 10 eV the CO molecules is destroyed by dissociative electron attachment (Laporta et al. 2016). The products of irradiation can be sorted in three groups: carbon chains C_n, suboxides, C_nO, and C_nO_2 species (details on the reaction scheme can be found in Jamieson et al. 2006). CO_2 (ν_3 at 2346 cm^{-1}) is the most abundant product in all the experiments. The features at 2248, 2243, and 1981 cm^{-1}, are assigned to C_3O, C_3O_2, and C_2O, respectively. They are common to ultraviolet irradiation of a thick CO ice (Gerakines et al. 1996), X-ray irradiation (Ciaravella et al. 2016), and 5 keV radiolysis (Jamieson et al. 2006). In this latter experiment, longer chain products such as C_5O_2 and C_7O are also observed. The detection of C_7O_2 at 2115 cm^{-1} has been also reported in soft X-ray irradiation experiments of pure CO ices (Ciaravella et al. 2016). The non-detection of C_7O_2 by Jamieson et al. (2006) may be due to the blending of this feature with the CO–Ag band at 2112 cm^{-1}. The carbon chains C_8 and C_9 are obtained in X-ray irradiation experiments, but not mentioned in Jamieson et al. (2006). Finally the unknown features at 1578, 2045, 2049, 2153, 2173, and 2235 cm^{-1} have been also reported in Ciaravella et al. (2016). The products of the irradiation are summarized in Table 2, where we report the wavenumber, the assignment, the band strength (whenever available), the lowest energy experiments in which the product has been detected, and the references.

We plot the column densities of six products of the irradiation as functions of the absorbed energy in Figure 3. We define the absorbed energy as $E_e \times F$, where $F = f \times t$ is the fluence measured in number of electrons per cm^2, and t the irradiation time. Multiple Gaussian fitting has been used to compute C_2O and C_3 column densities because of the blending with nearby features.

Increasing the electron energy, the maximum value of CO_2 column density $N^{(m)}_{CO_2}$ increases, and shifts toward higher absorbed energies (see Figure 3). For instance, in the 200 eV electron

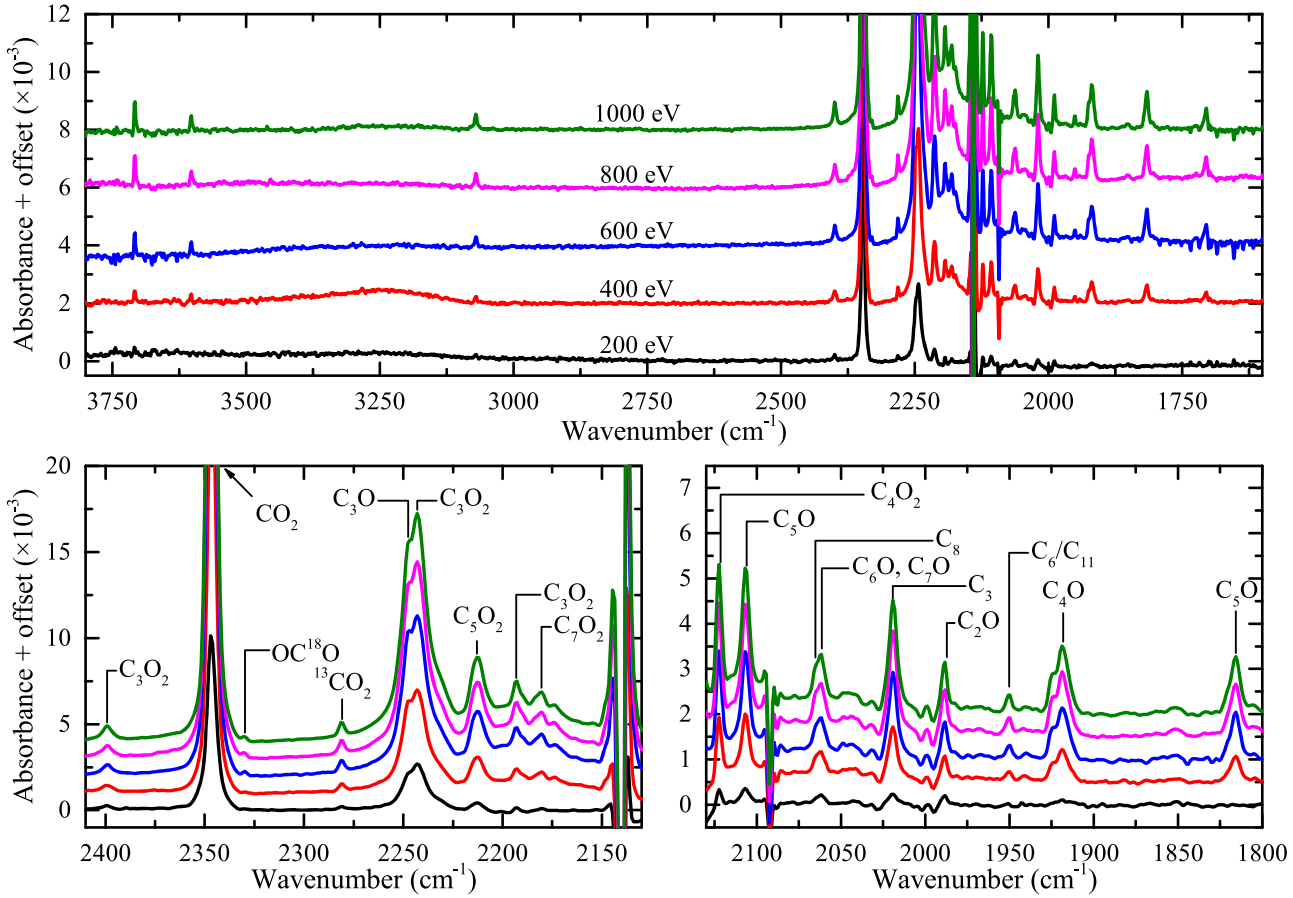

Figure 2. Infrared spectra of the CO ice after radiolysis with electrons of 200 (black), 400 (red), 600 (blue), 800 (pink), and 1000 (dark green) eV. The spectra are obtained as differences between the irradiated and the sample spectra. The top panel shows the spectra in the range of 3800–1600 cm^{-1}, while the bottom panels show the detailed region from 2410 to 1800 cm^{-1}. Main products are marked.

experiment, $N^{(m)}_{CO_2} = 0.8$ ML is located at 6×10^{16} eV cm^{-2}, while in the 1000 eV experiment $N^{(m)}_{CO_2} = 3.2$ ML is reached at 2×10^{17} eV cm^{-2}. This behavior is also observed for other species, see e.g., C_3, C_5O, and C_4O_2.

The maximum values of the column densities as functions of the electron energy for CO_2, C_3, and C_5O are shown in Figure 4. The $N^{(m)}$ increases almost linearly with the electron energy up to 250 eV; then, at higher energies the linear regime breaks down and the maximum column densities tend to saturate.

4.2. CO Destruction Cross Section

The destruction of CO during the irradiation is shown in Figure 5. Since the CO stretching band at 2136 cm^{-1} is close to saturation, we choose to compute CO column densities using the ^{13}CO isotopologue.

The destruction cross section of CO can be derived from the following equation

$$dn_{CO}(s, t) = -n_{CO}\sigma_D f(s, t)dt, \quad (2)$$

where dn_{CO} is the number density of destroyed CO molecules, n_{CO} the CO number density, σ_D the destruction cross section, and $f(s, t)$ the electron flux along the penetration path. Since only 4% of the initial number density of CO is converted into new species, we assume n_{CO} is constant within the ice. Integrating Equation (2) along the penetration path we obtain

$$dN_{CO}(t) = -n_{CO}\sigma_D \int_0^{\Lambda_e} f(s, t)\, ds\, dt, \quad (3)$$

where we indicate with N_{CO} the CO column density. Finally, the destruction cross section is defined as

$$\sigma_D = -\frac{\Delta N_{CO}}{n_{CO}\int_0^{\Lambda_e} F(s)ds}, \quad (4)$$

where ΔN_{CO} is the column density of destroyed CO. We use CASINO to evaluate $\int_0^{\Lambda_e} F(s)ds$ for each electron energy.

The cross section, σ_D, as a function of the electron energy is shown in Figure 6. This quantity has a broad peak centered around 250 eV, and it shows similarities in shape with the electron-impact ionization cross section of gas-phase CO (e.g., Chung 2002, and references therein), whose peak is instead located at a lower energy, 120 eV. The destruction cross section for CO ice is about one order of magnitude larger than that obtained for gas-phase.

4.3. CO_2 Production Cross Section

We derive the production cross section of carbon dioxide, $\sigma^{(1)}_f$, through a fitting relation that takes into account only production processes, i.e considering a first-order kinetic

Table 2
Products

Wavenumber (cm^{-1})	Assignment	Band Strength (cm $molecule^{-1} \times 10^{-17}$)	Lowest Energy Detection (eV)	References
3741	C_3O_2		800	
3707	CO_2		150	Gerakines et al. (1995, 1996)
3601	CO_2		300	Gerakines et al. (1995, 1996)
3069	C_3O_2		150	Gerakines & Moore (2001), Miller & Fately (1964)
2399	C_3O_2	0.8	150	Gerakines & Moore (2001), Miller & Fately (1964)
2346	CO_2	7.6	150	Yamada & Person (1964)
2330	$OC^{18}O$		150	Falk (1987)
2281	$^{13}CO_2$	7.8	150	Gerakines et al. (1995)
2248	C_3O		150	DeKock & Weltner (1971)
2243	C_3O_2	1.3	150	Miller & Fately (1964), Hayden Smith & Leroy (1966), Gerakines & Moore (2001)
2235	...		150	Ciaravella et al. (2016)
2212	C_5O_2		150	Holland et al. (1988), Maier et al. (1988)
2194	C_3O_2		150	Brown et al. (1985)
2190	C_7O_2 (C_3O_2)		150	Maier et al. (1991)
2183	C_7O_2		200	Maier et al. (1991)
2173	...		200	Ciaravella et al. (2016)
2163	C_5 (C_6O)		150	DeKock & Weltner (1971), Dismuke et al. (1976), Maier et al. (1991)
2153	...		150	Ciaravella et al. (2016)
2139[a]	CO	1.1		Jiang et al. (1975), Hudgins et al. (1993)
2122	C_4O_2 (C_7O_2)	25.0	150	Kim et al. (1998), Maier et al. (1988)
2115	C_7O_2		150	Maier et al. (1991)
2106	C_5O/C_3O_2		150	Jamieson et al. (2006), Gerakines & Moore (2001)
2092[a]	^{13}CO	1.3		Gerakines et al. (1995)
2088[a]	$C^{18}O$			
2077	C_3O_2 (C_9, C_{10})		150	Jamieson et al. (2006), Van Orden et al. (1996) Freivogel et al. (1997)
2065	C_8		150	Freivogel et al. (1997)
2062	C_6O/C_7O (C_5O_2)		150	Holland et al. (1988), Maier et al. (1988)
2058	C_5O_2		150	Jamieson et al. (2006), Maier et al. (1988)
2049	...		150	Ciaravella et al. (2016)
2045	...		150	Ciaravella et al. (2016)
2019	C_3	10.0	200	Hutter et al. (1994)
1988	C_2O		150	Jamieson et al. (2006), DeKock & Weltner (1971), Jacox & Milligan (1965), Gerakines et al. (1996)
1981	C_2O		150	Jamieson et al. (2006)
1969	C_2O		500	Jacox & Milligan (1965)
1951	C_6 (C_{11})		250	Kranze & Graham (1992), Tam et al. (1997)
1939	C_{10} (C_{11})		300	Freivogel et al. (1997)
1924	C_4O		200	Maier et al. (1988)
1918	C_4O		200	Maier et al. (1988), Dibben et al. (2000)
1816	C_5O (C_{12})	6.2	250	Jamieson et al. (2006), Ding et al. (2000)
1704	C_8		400	Freivogel et al. (1997)
1697	C_7O_2		400	Maier et al. (1991)
1592	C_9		400	Kranze et al. (1995)
1578	...		500	Ciaravella et al. (2016)
1563	C_3O_2		400	Wang et al. (2002), Jamieson et al. (2006)
1274	CO_2		600	Gale et al. (1985)
1145	C_5O_2		1000	Maier et al. (1988)

Note
[a] parent molecule.

process (Mennella 2010),

$$N_{CO_2} = N_{CO_2}^{(m)} \times (1 - e^{-\sigma_f^{(1)} F}), \quad (5)$$

where F is the number of electrons per cm^2 at a given irradiation time. This fit has been obtained using the column density profiles up to their maximum values $N_{CO_2}^{(m)}$. The resulting production cross section is shown in Figure 7. The cross section exhibits a dip between 400 and 500 eV. Such a feature has been confirmed by repeating the experiment, and fitting the results. We discuss this point in Section 5.

To test the robustness of this result, we also estimate the production cross section using the consecutive reaction formalism:

$$2\,CO \xrightarrow{\sigma_f} CO_2 + C \xrightarrow{\sigma_d} CO + O + C, \quad (6)$$

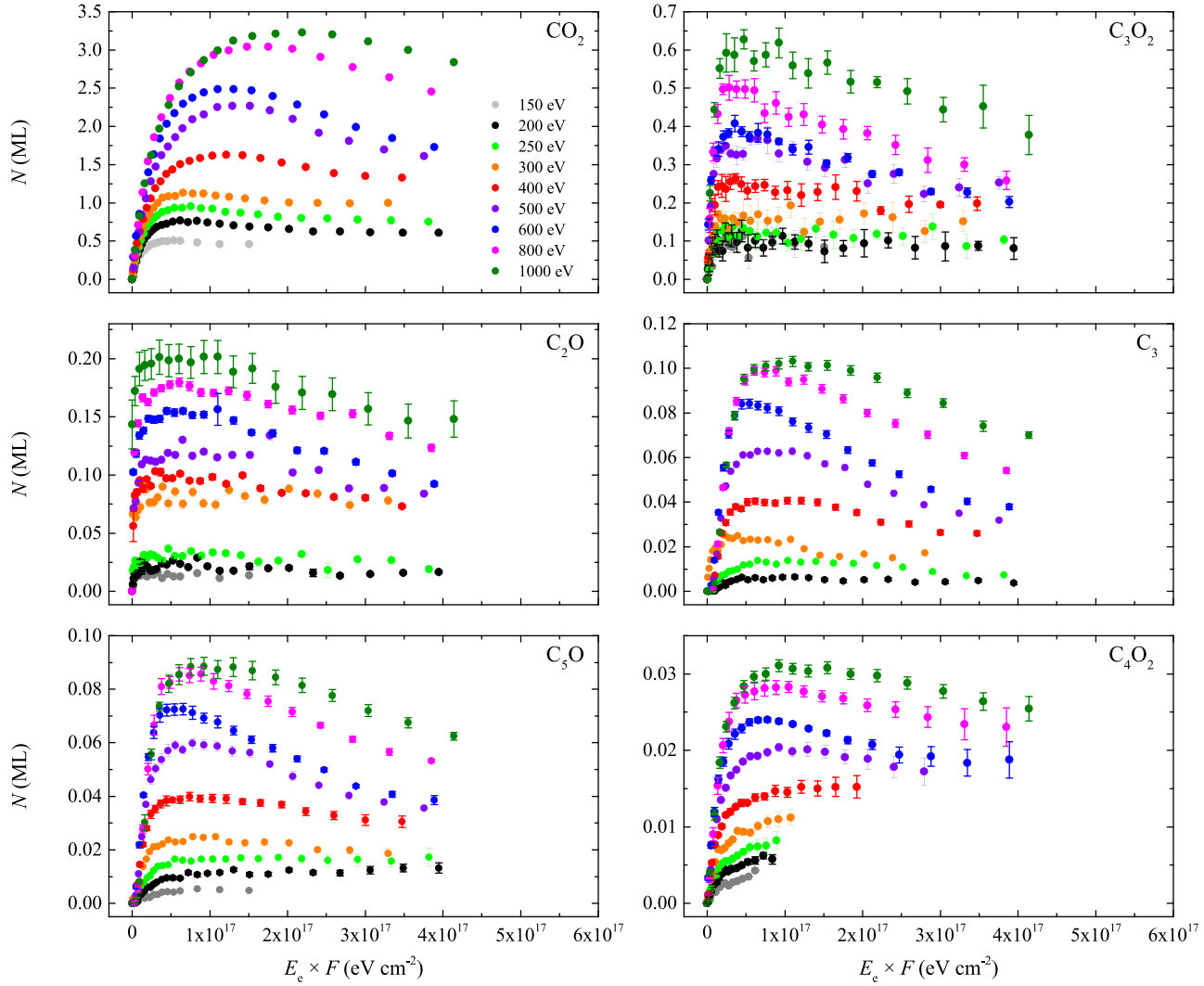

Figure 3. Column density vs. absorbed energy for CO_2, C_3O_2, C_2O, C_3, C_5O, and C_4O_2. The different colors are for electrons of 150 (gray dots), 200 (black), 250 (light green), 300 (orange), 400 (red), 500 (purple), 600 (blue), 800 (pink), and 1000 eV (dark green).

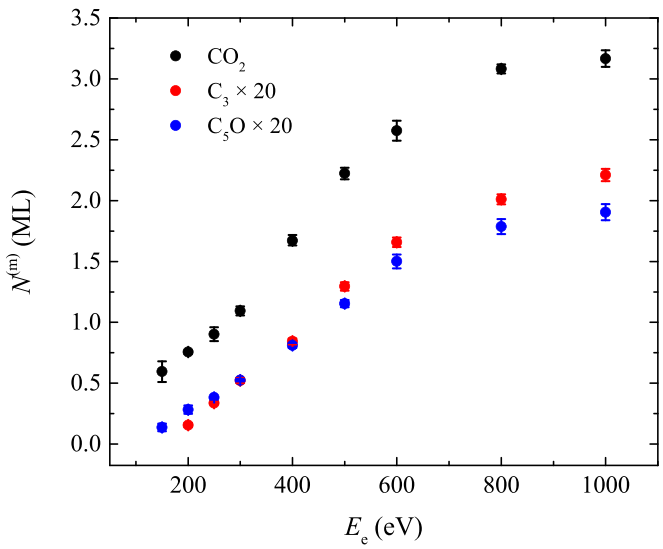

Figure 4. Maximum column density of CO_2, C_3, and C_5O vs. electron energy. The column densities for C_3, and C_5O are multiplied by factor of 20.

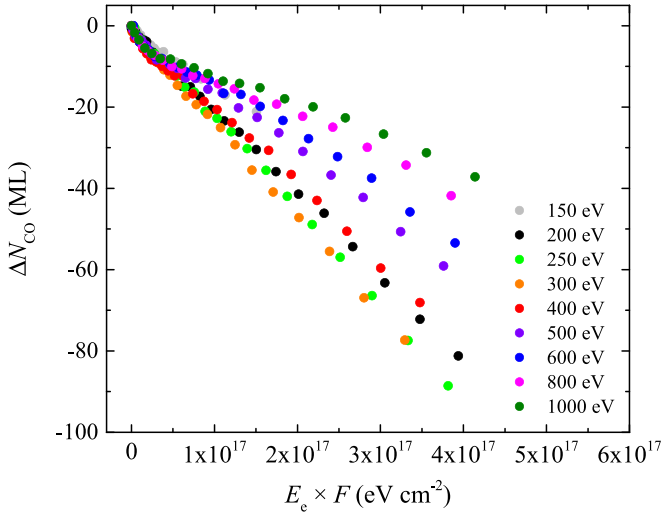

Figure 5. CO column density estimated from ^{13}CO vs. the absorbed energy during the irradiation of 150 (gray dots), 200 (black), 250 (light green), 300 (orange), 400 (red), 500 (purple), 600 (blue), 800 (pink), and 1000 eV (dark green) electrons.

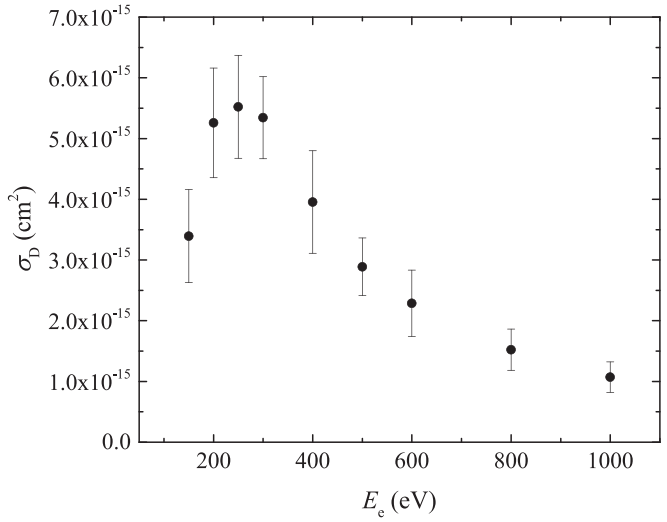

Figure 6. CO destruction cross section as a function of the electron energy. $\pm 1\sigma$ error bars are plotted.

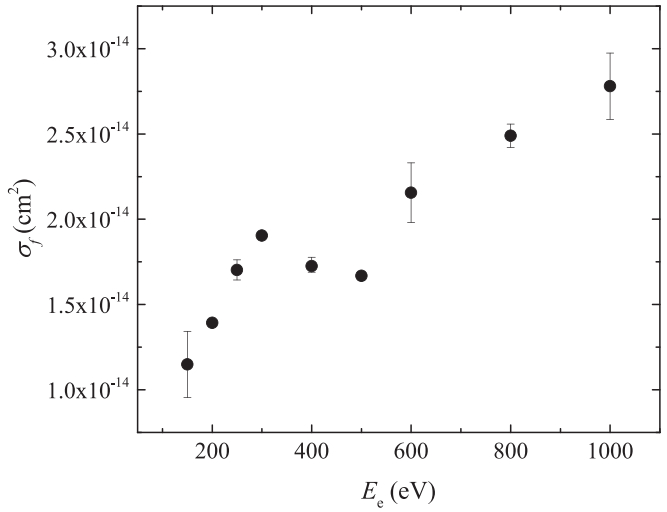

Figure 7. CO_2 production cross section as function of the energy of the impacting electrons. 1 σ error bars are plotted.

$$N_{CO_2} = N_{CO_2}^{\infty} + Ae^{-\sigma_d^{(2)}F} - Be^{-\sigma_f^{(2)}F}, \quad (7)$$

where $N_{CO_2}^{\infty}$ is the asymptotic column density for very high fluences, $\sigma_f^{(2)}$ and $\sigma_d^{(2)}$ are the production and destruction cross sections, and A and B are two fitting parameters. We obtain values very similar to $\sigma_f^{(1)}$. The destruction cross section $\sigma_d^{(2)} = (2\text{–}3) \times 10^{-15}\,\mathrm{cm}^2$ should be taken as an order of magnitude estimate because of the limited energy range exploited to trace the decline of N_{CO_2} (e.g., in 1000 eV experiment we have just four points after the peak).

4.4. CO and CO_2 Desorption

During radiolysis experiments the QMS detected a few species desorbing the ice that included both the parent CO and products. Among the products, the strongest detected signal is coming from CO_2 ($m/z = 44$), the major reaction product of the irradiation. We assume that this mass is produced entirely by CO_2. Such an approximation is justified by the negligible

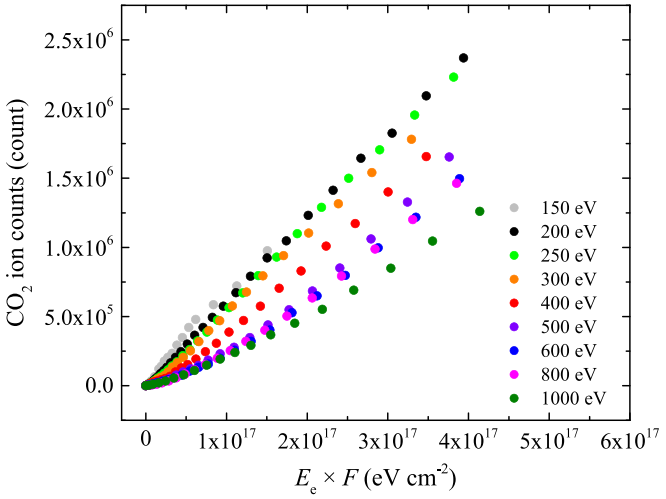

Figure 8. CO_2 ($m/z = 44$) accumulated ion counts as functions of the absorbed energy during radiolysis experiments exploiting electrons of 150 (gray dots), 200 (black), 250 (light green), 300 (orange), 400 (red), 500 (purple), 600 (blue), 800 (pink), and 1000 eV (dark green).

desorption of the second major product C_3O_2. In Figure 8 the accumulated ion count profile for $m/z = 44$ as a function of the absorbed energy is shown. The accumulated counts increase with increasing absorbed energy, and decrease with the energy of the impacting electrons, in qualitative agreement with the measurements of the electron-stimulated desorption yields performed by Tratnik et al. (2007). We compute the average desorbing yield, Y, using the accumulated ion counts, $\mathcal{K}$, as

$$Y(E_e) = \frac{1}{E_e}\left\langle \frac{d\mathcal{K}}{dF} \right\rangle_{\mathrm{irr}}. \quad (8)$$

In the left panel of Figure 9 the desorption yield of CO decreases with increasing electron energy.

The CO_2 and CO desorption yields are compared in the right panel of Figure 9. The yields are positively correlated suggesting that CO_2 co-desorbs with the much more abundant CO.

4.5. The Role of Ice Thickness

The effects of ice thickness on the chemical evolution have been explored by running additional experiments with electrons of 200, 400, 600, 800, and 1000 eV on a 76.9 ± 0.5 ML (34.7 ± 0.2 nm) ice. The CO_2 peak production is very similar for low-energy electrons, while for energies higher than 600 eV, the production in thin ices declines. This is clearly proven in Figure 10 where maximum CO_2 column densities in both thin (~80 ML) and thick (~800 ML) irradiated ices are compared.

The difference in $N_{CO_2}^{(m)}$ increases with the energy of the electrons. For 1000 eV electrons $N_{CO_2}^{(m)}$ results are approximately 30% higher in the thick irradiated ice. It is worth noting that for each electron energy, the maximum of CO_2 column density occurs at the same absorbed energy for both thicknesses. A similar behavior has been detected in 1 keV electron irradiation experiments of a pure NH_3 ice (Shulenberger et al. 2019).

The CO destruction in the thin ice experiments is reported in Figure 11. The behavior of the CO column density as a function of the electron energy is similar to that observed in thick ices. Most destruction occurs in the lowest electron

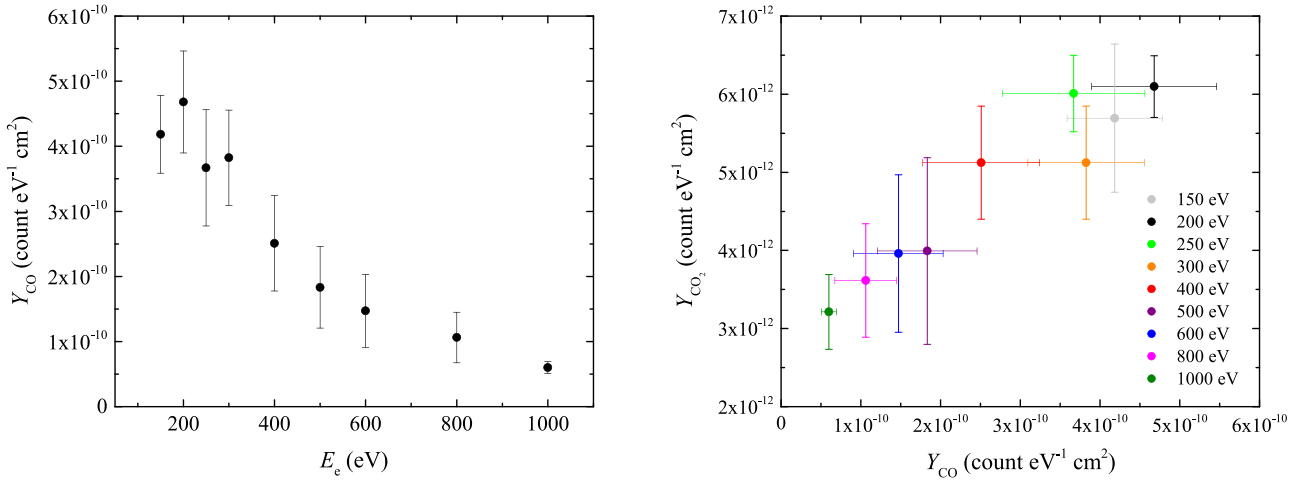

Figure 9. Left panel: CO desorption yield as a function of the electron energy. Right panel: comparison between CO and CO_2 desorption yields for 150 (gray), 200 (black), 250 (light green), 300 (orange), 400 (red), 500 (purple), 600 (blue), 800 (pink), 1000 (dark green) eV electrons. $\pm 1\sigma$ error bars are plotted.

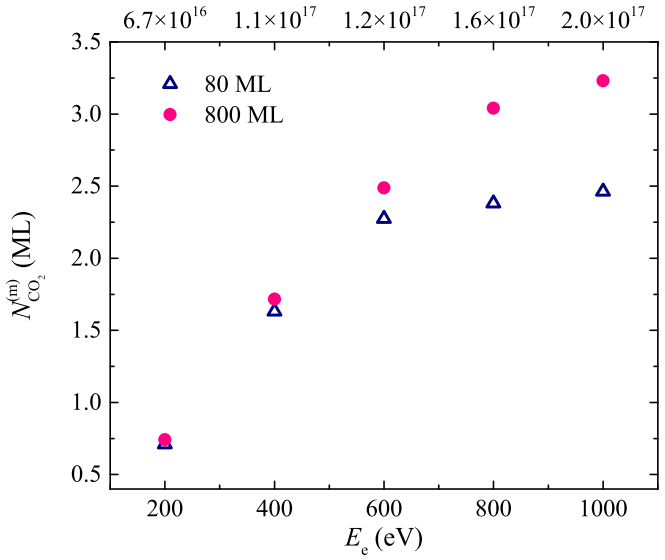

Figure 10. Maximum CO_2 column density as a function of the electron energy (bottom axis) and absorbed energy (top axis) for CO ice thicknesses of 80 (blue triangles) and 800 (red dots) ML.

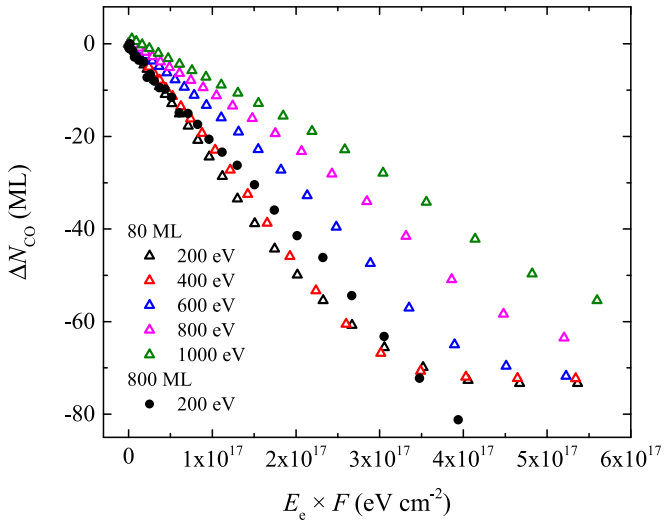

Figure 11. Destroyed CO column density as function of absorbed energy for 200 (black), 400 (red), 600 (blue), 800 (pink), 1000 (dark green) eV electrons in 80 ML (empty triangle) ice. The solid black dots refer to 200 eV electrons in 800 ML ice as from Figure 3.

energy experiments. The main difference is the saturation at low energies where the ice is almost totally destroyed. For comparison we report the 200 eV experiment in thick ice (black dots), in which at 3.5×10^{17} eV cm^{-2} only 10% of the initial CO column density is destroyed and saturation does not occur.

5. Discussion

In this work we study the chemical evolution of pure CO ices irradiated by electrons in the 150–1000 eV range. The inventory of reaction products does not change with the energy of the impinging electrons. As for other energetic sources (e.g., ultraviolet photons or X-rays), the most abundant species is CO_2. The fraction of destroyed CO going into the formation of products increases with the electron energy. When CO_2 reaches its peak abundance, this fraction is 0.17–0.4 (from 150 eV–1000 eV). For instance, in the 1000 eV experiment the CO_2 peak column density is 3.2 ML against 20 ML of destroyed CO. This means that approximately 30% of the destroyed CO is used for CO_2, while only 10% for other (minor) products. The remaining 60% is mostly desorbed, with a fraction dissociated into C + O. According to Jamieson et al. (2006) this fraction cannot be large, because O_2 and O_3, produced through barrierless reactions, would be otherwise detected (while they are not).

CO_2 column densities exhibit a broad maximum, that raises and steepens with the energy of the impacting electrons. The absorbed energy (eV cm^{-2}) at which the CO_2 column density peak is attained, increases as well.

The results of the experiment performed with $E_e = 400$ eV appear to separate two different regimes. This behavior is reflected by the shape of the CO_2 production cross section (see Figure 7) that shows a peak at 300 eV, a dip at about 500 eV, and a convex rise toward higher energies. The peak energy is close to the maximum of the CO destruction cross section (Figure 6). The cross section after reaching its maximum value at about 250 eV decreases steadily for higher energies. This might appear inconsistent with the high energy rise of CO_2 production cross section. These two seemingly conflicting

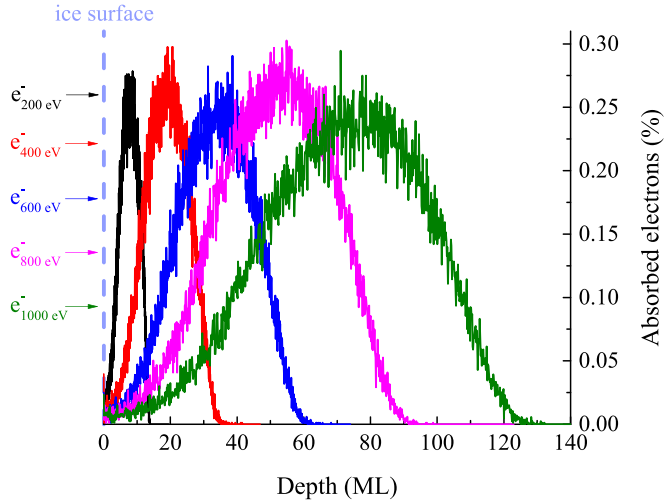

Figure 12. Histogram of electron distributions as obtained from CASINO across the CO ice. The right vertical axis shows the percentage of the absorbed electrons. Different colors indicate different electron energies, see left vertical axis. The number of bins in each histogram is 1000, and the total number of electrons is normalized to unity.

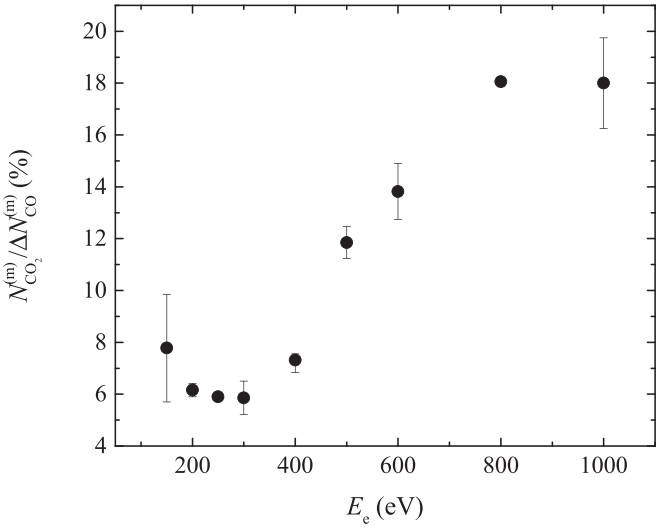

Figure 13. The ratio between the maximum column density of produced CO_2 ($N^{(m)}_{CO_2}$) and the corresponding destroyed column density of CO ($\Delta N^{(m)}_{CO}$) as a function of the electron energy E_e.

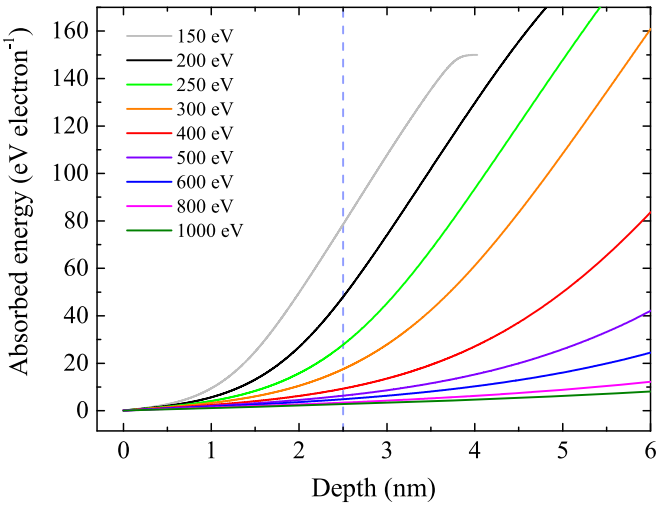

Figure 14. Energy deposited by electrons of different energies close to the ice boundary (obtained from CASINO).

results may be reconciled once we take into account CO and CO_2 desorption induced by the electron irradiation.

In Table 1 we list the electron penetration depth, Λ_e for each electron energy. This quantity, derived using the CASINO software, increases quadratically with the energy of the impacting electron, and it is a measure of the ice thickness that is being processed by electrons of specific energies. The absorbed electron distribution within the ice has been computed from CASINO and it is shown in Figure 12. As the figure shows, the electron distribution inside the ice displays an asymmetric bell-shaped profile, peaking at a distance from the ice edge $\sim 2/3 \times \Lambda_e$. The CO_2 produced during the irradiation follows the electron distribution. Thus, the CO_2 production is increasingly affected by desorption, as the energy of the impacting electrons decreases.

At a specific location in the ice, the CO_2 concentration is determined by both chemistry and ice erosion. If the corresponding timescales are comparable, the measured CO_2 column density is continuously produced over the desorption timescale, as new ice layers are processed by electrons. In fact, at low electron energies where the timescale of production and erosion are comparable we detect shallow peaks followed by a smooth decline of CO_2 (see Figure 3). As a consequence, the CO_2 production cross section mirrors the trend in CO destruction, i.e., peaking at about 300 eV and then declining. In this regime, the maximum produced CO_2 column density, $N^{(m)}_{CO_2}$, is directly proportional to the column density of destroyed CO, $\Delta N^{(m)}_{CO}$. As the electron energy increases, the electron distribution widens (see Figure 12), decreasing significantly the number of electrons close to the ice edge, reducing desorption. The average power density $P_e = E_e \times f/\Lambda_e$ decreases due to the much larger spread along the electron penetration path. As a consequence, the CO_2 column density begins to accumulate, following the increase of ice layers involved in the CO_2 production with respect to the ones removed by desorption events. Thus, the production cross section rises with the electron energy in response to the increase of Λ_e, and so does the $N^{(m)}_{CO_2}/\Delta N^{(m)}_{CO}$ ratio (Figure 13).

In Figure 14 we show the energy deposited by electrons of different energies as a function of the penetration within the ice. For all locations the amount of deposited energy decreases monotonically with increasing energy of the impacting electrons. At 2.5 nm, a distance lower than the penetration depth of the lowest energy electron considered in this work, 150 eV electrons deposit 78 eV, while 1000 eV electrons just 3 eV.

Finally, when the thickness of the ice is comparable with the penetration depth, the abundances of products decrease with respect to the case of a thicker ice.

For electrons with higher energies, the penetration depth increases significantly. In the case of 5 keV electrons used by Jamieson et al. (2006) the penetration depth, $\Lambda_e \sim 1500$ ML, is about one order of magnitude larger than for 1 keV electrons (see Table 1). Extrapolating the results of our experiments to the case of 5 keV electron irradiation we may expect a significantly lower desorption (per eV), consequently a richer chemical production, and the CO_2 column density peak located at a much larger absorbed energy. This is qualitatively in agreement with the findings of Jamieson et al. (2006).

We compare our results with those found by Jamieson et al. (2006). The two experiments differ in the sample sizes that are 3 cm^2 and (2 ± 0.1 cm^2), in Jamieson et al. (2006) and in the present work, respectively. Moreover, Jamieson et al. (2006) scanned over the sample area while we irradiate in a single spot. Extrapolating the data shown in Figure 10 up to 5 keV, we obtain $N_{CO_2}^{(m)} \sim 5.5$ ML. Jamieson et al. (2006) derive a best-fit value for this quantity as $N_{CO_2}^{(m)} \sim 5.8$ ML, in remarkable agreement with the present results.

6. Conclusions

In this work we have performed electron-impact experiments on pure CO ices. Both CO ices and fast electrons are ubiquitous in space, from dense molecular clouds to planetary surfaces. We employ electrons in the middle-energy range (150–1000 eV) in order to fill the gap existing in previous experiments adopting relatively high energy electrons (Jamieson et al. 2006) or studying low-energy (1–30 eV) electron interactions with CO such as dissociative electron attachment (Munro et al. 2012). Our assumed range of energy is also close to the energy distribution of primary electrons emitted in the interaction of cosmic-rays and X-rays with molecular gas (Dalgarno et al. 1999).

The main results of this work are as follows:

1. the identification of new formed species provides an inventory very close to the one resulting from X-ray irradiation, confirming the driving role of secondary electron cascade in the chemistry of the ice;
2. we provide the evolutionary tracks of products and find that major products (i.e., CO_2, C_3, C_5O) evolve following similar patterns;
3. CO desorption is relevant, eroding significantly the ice upon long irradiation time;
4. CO destruction cross section, CO_2 production cross section, CO and CO_2 desorption yields have been determined; the shape of CO_2 production cross section reflects the competition between chemistry and desorption;
5. CO_2 molecules (and presumably all the other products) co-desorb with CO ice, with the yields declining with increasing electron energy (penetration depth);
6. extrapolation of the present results to higher energy provide a good agreement with the results of 5 keV electron experiments performed by Jamieson et al. (2006).

The chemistry that we observe to occur in CO ice under electron processing may have implications in the atmospheric photochemistry of cold planets hosting surface CO ices. A few years ago, Lellouch et al. (2010) discovered a seasonal evolution of Triton's atmosphere over decades. Something similar has been observed taking place on Pluto (Bertrand & Forget 2016). Volatile chemicals such as nitrogen, methane, and carbon monoxide start out as ices on the surface, then sublime into the atmosphere when temperatures rise. Solar wind electrons (Hoogeveen & Cloutier 1996) and/or primary electrons produced by cosmic-rays inducing a chemistry such as the one we have described in this work, may contribute to enrich the nitrogen-rich atmosphere of these small planets with suboxides and carbon chains (in addition to CO_2). As volatile gases drift upwards, photochemical reactions create new carbon and nitrogen compounds. Moreover, carbon chains at the boundary layer may assemble and combine into solid carbonaceous matter at cryogenic temperature, as has been shown in a recent experiment by Fulvio et al. (2017), forming nano-sized particles. These particles settle down onto the planets's surface, and coat it until warming begins and they are lofted into the atmosphere.

This work has been supported by the project MOST grants MOST 107-2112-M-008-016-MY3 (Y.-J.C.), Taiwan. We also acknowledge support from INAF through the PRIN-INAF 2016 The Cradle of Life—GENESIS-SKA (General Conditions in Early Planetary Systems for the rise of life with SKA).

ORCID iDs

C.-H. Huang https://orcid.org/0000-0003-2741-2833
A. Ciaravella https://orcid.org/0000-0002-3127-8078
C. Cecchi-Pestellini https://orcid.org/0000-0001-7480-0324
A. Jiménez-Escobar https://orcid.org/0000-0003-3360-9333
N.-E. Sie https://orcid.org/0000-0001-7755-7884
Y.-J. Chen https://orcid.org/0000-0003-4497-3747

References

Beaulieu, J. P., et al. 2006, Natur, 439, 437
Bertrand, T., & Forget, F. 2016, Natur, 540, 86
Boogert, A. C. A., Gerakines, P. A., & Whittet, D. C. B. 2015, ARA&A, 53, 541
Brown, R., Pullin, D., Rice, E., & Rodler, M. 1985, JAChS, 107, 7877
Cecchi-Pestellini, C., & Aiello, S. 1992, MNRAS, 258, 125
Chen, Y.-J., Chuang, K.-J., Caro, G. M., et al. 2014, ApJ, 781, 15
Chuang, K.-J., Fedoseev, G., Ioppolo, S., van Dishoeck, E. F., & Linnartz, H. 2016, MNRAS, 455, 1702
Chung, Y.-S. 2002, JKPS, 41, 682
Ciaravella, A., Chen, Y.-J., Cecchi-Pestellini, C., et al. 2016, ApJ, 819, 38
Cruz-Diaz, G. A., Muñoz Caro, G. M., Chen, Y.-J., & Yih, T.-S. 2014, A&A, 562, A119
Dalgarno, A., Yan, M., & Liu, W. 1999, ApJS, 125, 237
DeKock, R., & Weltner, W. 1971, JAChS, 93, 7106
Dibben, M., Szczepanski, J., Wehlburg, C., & Vala, M. 2000, JPCA, 104, 3584
Ding, X. D., Wang, S. L., Rittby, C. M. L., & Graham, W. R. M. 2000, JChPh, 112, 5113
Dismuke, K. I., Graham, W. R. M., & Weltner, W., Jr. 1976, ApJ, 204, 301
Drouin, D., Couture, A. R., Joly, D., et al. 2007, Scanning, 29, 92
Falk, M. 1987, JChPh, 86, 560
Freivogel, P., Grutter, M., Forney, D., & Maier, J. P. 1997, CP, 216, 401
Fulvio, D., Góbi, S., Jäger, C., Kereszturi, Á., & Henning, T. 2017, ApJS, 233, 14
Gale, G. M., Guyot-Sionnest, P., Zheng, W. Q., & Flytzanis, C. 1985, PhRvL, 54, 823
Gerakines, P. A., & Moore, M. H. 2001, Icar, 154, 372
Gerakines, P. A., Schutte, W. A., & Ehrenfreund, P. 1996, A&A, 312, 289
Gerakines, P. A., Schutte, W. A., Greenberg, J. M., & van Dishoeck, E. F. 1995, A&A, 296, 810
Gillett, F. C., & Forrest, W. J. 1973, ApJ, 179, 483
Hayden Smith, W. M., & Leroy, G. E. 1966, JChPh, 45, 1767
Herbst, E., & van Dishoeck, E. F. 2009, ARA&A, 47, 427
Holland, F., Winnewisser, M., Maier, G., Reisenauer, H., & Ulrich, A. 1988, JMoSp, 130, 470
Hoogeveen, G. W., & Cloutier, P. A. 1996, JGR, 101, 19
Hudgins, D. M., Sandford, S. A., Allamandola, L. J., & Tielens, A. G. G. M. 1993, ApJS, 86, 713
Hutter, J., Lüthi, H. P., & Diederich, F. 1994, JAChS, 116, 750
Jacox, M. E., & Milligan, D. 1965, JChPh, 43, 3734
Jamieson, C. S., Mebel, A. M., & Kaiser, R. I. 2006, ApJS, 163, 184
Jiang, G. J., Person, W. B., & Brown, K. G. 1975, JChPh, 64, 1201
Kim, K., Lee, B., & Lee, S. 1998, Bull. Korean Chem. Soc., 19, 553
Kranze, R. H., & Graham, W. R. M. 1992, JChPh, 96, 2517
Kranze, R. H., Withey, P. A., Rittby, C. M. L., & Graham, W. R. M. 1995, JChPh, 103, 6841
Lacy, J. H., Baas, F., Allamandola, L. J., et al. 1984, ApJ, 276, 533
Laporta, V., Tennyson, J., & Celiberto, R. 2016, PSST, 25, 06LT02
Lellouch, E., de Bergh, C., Sicardy, B., Ferron, S., & Käuf, H.-U. 2010, A&A, 518, L8
Maier, G., Reisenauer, H., Schäfer, U., & Balli, H. 1988, Angew. Chem. Int., 27, 566
Maier, G., Reisenauer, H. P., & Ulrich, A. 1991, Tetrahedron Letters, 32, 4469

Mennella, V. 2010, ApJ, 718, 867
Miller, F., & Fately, W. 1964, Spectrochim. Acta, 20, 253
Munro, J. J., Harrison, S., Fujimoto, M. M., & Tennyson, J. 2012, JPhCS, 388, 012013
Shulenberger, K. E., Zhu, J. L., Tran, K., et al. 2019, ECS, 3, 800
Tam, S., Macler, M., & Fajardo, M. 1997, JChPh, 106, 8955
Tiné, S., Lepp, S., Gredel, R., & Dalgarno, A. 1997, ApJ, 481, 282
Tratnik, H., Hillereta, N., & Störi, H. 2007, Vacuu, 81, 731
Van Orden, A., Provencaal, R. A., Keutsch, F. N., & Saykally, R. J. 1996, JChPh, 105, 6111
Wang, H.-Y., Lu, X., Huang, R.-B., & Zheng, L.-S. 2002, JMoSt, 293, 187
Yamada, H., & Person, W. B. 1964, JChPh, 41, 2478